

Holistic Multi-View Building Analysis in the Wild with Projection Pooling

Zbigniew Wojna,¹ Krzysztof Maziarz,^{*2} Łukasz Jocz,¹
Robert Pałuba,¹ Robert Kozikowski,¹ Iasonas Kokkinos³

¹ Tensorflight

² Jagiellonian University

³ University College London

Abstract

We address six different classification tasks related to fine-grained building attributes: construction type, number of floors, pitch and geometry of the roof, facade material, and occupancy class. Tackling such a remote building analysis problem became possible only recently due to growing large-scale datasets of urban scenes. To this end, we introduce a new benchmarking dataset, consisting of 49426 images (top-view and street-view) of 9674 buildings. These photos are further assembled, together with the geometric metadata. The dataset showcases various real-world challenges, such as occlusions, blur, partially visible objects, and a broad spectrum of buildings. We propose a new *projection pooling layer*, creating a unified, top-view representation of the top-view and the side views in a high-dimensional space. It allows us to utilize the building and imagery metadata seamlessly. Introducing this layer improves classification accuracy – compared to highly tuned baseline models – indicating its suitability for building analysis.

1 Introduction

This work aims to develop a deeper understanding of scenes containing buildings based on aerial (top-view) and multiple side view (street-view) images. This problem is both technically challenging and of great practical importance. It allows for automatic pricing of an insurance policy, mechanical claims analysis, risk detection, understanding the environment for self-driving cars, or socioeconomic statistics extraction. The onset of new computer vision techniques and growing large-scale datasets of urban scenes naturally lead to various new scientific challenges related to holistic building understanding, much deeper than simple single-task classification. We investigate a multi-task classification problem of automated building analysis. The goal is to determine the following set of building attributes: construction type, i.e., the material the building is made of, number of floors, roof pitch, roof geometry, facade material, and occupancy type. Those features are crucial for catastrophic risk estimation (Stone 2018). The real-world unconstrained environment is often poorly recognizable based on a single image. Rather, it requires more complex analyses of multiple

images taken from different angles. Our model uses both the top-view image and numerous street-view photographs of the same building to understand its fine-grained details.

In this work, we propose a new fusion technique, leveraging both the scene’s geometric structure and the high-dimensional features extracted from the top and street-view images. As a result, we obtain a single unified top-view representation of the scene, including information from side views, building outline, and imagery metadata. Based on the street-view photo location, direction, and the field of view, i.e., angle representing the visible range, we construct a projection of the street-view features onto the building walls outlined in the top-view image.

Understanding of physical structures, such as buildings, may require integrating information from all possible input sources. An example of a *building scene* from our dataset is presented in Figure 1. The four camera marks on the top-view image represent four different locations where the street-view images were taken. The green mark and the blue boundary on the top-view image point to the building of interest. The violet boundaries represent other visible buildings, which can be a source of confusion for the model. We can easily see how different images complement each other. The top-view image allows us to see that the roof is not flat as there is a ridge joining the two opposite sides and a skewed shadow. The roof geometry is only visible from the top-view image. The construction type, number of floors, facade material, and occupancy class can be determined only based on the street-view images.

Some decisions may require more sophisticated reasoning. A possible overlap of the features from different street-view photos might mitigate the errors caused by occlusions and inaccuracies present in a single image. In the example in Figure 1, the first street-view image points towards the center of the building but is occluded by an adjacent building and could lead to classification errors. However, when looking at all four images, it is possible to classify the building’s attributes correctly by combining several clues. The side-attached structure made of bricks may correctly suggest that all buildings’ construction type along the street is masonry. We are not able to estimate the exact roof pitch by looking exclusively at the street-view images. We can only assume that the roof is flat or has a low slope as it does not stick out from the front.

^{*}Work done during an internship at Tensorflight. The author is now at Microsoft Research.

Copyright © 2021, Association for the Advancement of Artificial Intelligence (www.aaai.org). All rights reserved.



Figure 1: An example of a challenging building scene in our dataset. We aim to answer multiple questions about the building, and the answer to each lies in a different input image. The green mark represents the source location of the bottom right image number 4, while the green rays represent its field of view. The building of interest is marked with a green pointer on the top-view image, and it is the white one on the side view. The shading on the top-view image reveals that the roof is not flat, and the geometry is a gable. The front wall occludes most of the roof, but we can still infer its low pitch. The first image is not precisely calibrated and could suggest wrong answers, but combining information from all the sources should prevent it.

To summarize, our contributions are the following:

(1) We propose a new layer called *projection pooling*, which benefits from the building scene geometry and the relationship between images from different views and perspectives. We then integrate it into a deep learning architecture. It results in a new, unified, high-dimensional representation and suits well the classification task.

(2) We develop a new deep convolutional model, fusing multiple inputs to understand building characteristics better. It includes the projection pooling layer and achieves results that are superior to highly tuned baseline models. These results indicate that one can design substantially more accurate models by incorporating information from multiple images.

(3) We build a new real-world multi-view multi-task dataset of building images, annotations, and attributes. Buildings are heterogeneous in architectural style, size, age, and come from all around the world. It sets a new benchmark of detailed building understanding to spark further research in this area.

2 Related work

In this section, we discuss the ideas which inspired this work. These include (a) the use of street-view images, (b) building modeling, (c) the fusion of street-view and top-view imagery, and (d) building attribute classification.

(a) As street-view imagery is becoming more ubiquitous, it brings new research opportunities. One can assess socioeconomic statistics (Gebru et al. 2017a,b), evaluate the safety, beauty and popularity of the neighborhood (Andersson, Birck, and Araujo 2017; Dubey et al. 2016), estimate the road safety (Song et al. 2018), perform road scene segmentation (Cordts et al. 2016), and determine precise geolocation of the car (Armagan et al. 2017a; Hirzer et al. 2017; Armagan et al. 2017b). Combining house rental ads and street-view imagery allows for performing 3D building reconstruction (Chu et al. 2016). In our work, we show

that street-view images can also help with understanding the state of urban structures.

(b) Building facade segmentation is a well-studied problem on 2D images (Yang and Förstner 2011; Tyleček and Šára 2013; Riemenschneider et al. 2012; Teboul et al. 2011; Martinovic and Van Gool 2013; Kozinski et al. 2015; Mathias, Martinović, and Van Gool 2016; Liu et al. 2017), through combination of 2D and 3D (Gadde et al. 2017; Riemenschneider et al. 2014) and directly using 3D data from scanners (Serna, Marcotegui, and Hernández 2016; Li et al. 2016). Many methods rely on assuming symmetry of the building facades (Cohen et al. 2017; Mitra et al. 2012; Musialski et al. 2009; Wu, Frahm, and Pollefeys 2010; Zhang et al. 2013). Facade datasets are usually collected at a specific location, consist only of a few hundred images, are homogeneous in style and well rectified. Therefore, models can fail when tested on different architectural styles (Lotte et al. 2018). Our work introduces a diverse and large-scale dataset, with buildings coming from all over the world, along with potential noise, and without any assumption about rectification, symmetry or style.

(c) A fusion of street-view and top-view imagery may further improve performance. One can fuse top-view and ground-level imagery for detailed city reconstruction (Bódis-Szomorú, Riemenschneider, and Van Gool 2016), use cross-view matching with top-view images to improve street-view geolocation (Workman, Souvenir, and Jacobs 2015; Hu et al. 2018), or use cross-view matching with street-view to retrieve latent representation of top-view images (Workman et al. 2017; Cao et al. 2018). In (Zhai et al. 2017), the authors transform a semantic top-view scene into a semantic street-view scene. Detecting trees can be achieved through merging both of these sources (Wegner et al. 2016). Projecting the street-view latent representation onto an orthographic projection allows for 3D object detection (Roddick, Kendall, and Cipolla 2019). MVSNet (Yao et al. 2018) introduces ‘differentiable homography’,

our layer is a special case of theirs, but we can utilize multiple images in a single training iteration and encode problem constraints directly in the model. Our solution also takes advantage of both input modalities but focuses on detailed building understanding. As opposed to the previous works, our fusion strategy directly utilizes the building geometry to create a 2D latent representation through the projection pooling layer.

(d) Closely related to our study is the classification of building age, condition, and land use from a single street-view image (Zeppelzauer et al. 2018; Koch et al. 2018; Kang et al. 2018; Zhu, Deng, and Newsam 2019). Urban zone classification was also explored in multi-view settings (Srivastava et al. 2018; Hoffmann et al. 2019; Srivastava, Vargas-Muñoz, and Tuia 2019), which we use as our multi-view multi-task baseline models. We are the first to study buildings from all around the world, where multiple recognition tasks are trained together. Most importantly, we propose a new fusion strategy based on building geometry, which boosts our models’ classification accuracy.

3 Dataset

One of the goals of this study is to create the first large-scale benchmark of buildings that represent a diverse spectrum of architectural styles, locations, and building attributes. Building sizes vary: from small wooden houses, through churches made of brick, to extensive concrete manufacturing facilities. Thus, models trained on such a dataset should apply to any building in the world. We present the world heatmap of building sites in Appendix A.

Our dataset of top-view images was collected from Google Maps and Bing Maps, while the street-view photos come from Google Street View and Bing StreetSide. The resolution of top-view images is around 30 cm per pixel; see Appendix B for more information on aerial images’ resolution. We built a custom tool and annotated the georeferenced top-view images with the following set of classes: buildings, temporary structures, trees. We selected the georeferenced street-view photos based on tree locations and other buildings visible on the top-view image to account for potential occlusions. The images were selected to have the best building visibility and cover all sides of the building. For every building, we have one top-view image and between 1 and 9 street-view photos. Knowing the street-view images’ locations, we compute the field of view required for every image to capture the entire building. Since these locations can be imprecise, we set the actual field of view to be 20% broader to make sure the whole building is present in the photo. Top and street-view images usually come from different dates, but our annotators verified that both images refer to the same structure. We annotated construction type, number of floors, roof pitch, roof geometry, facade material, and occupancy type for every building of interest. Hired contractors double-checked all the annotations and building characteristics. Additionally, construction types were checked by a professional architect.

We classified the building attributes as follows (Stone 2018):

- the construction type describes the predominant material used for the building construction, and it consists of four classes: masonry, metal, reinforced concrete, and wood;
- the number of floors includes five categories: one, two, three, four and five or more;
- the roof pitch was divided into four categories: flat ($0^\circ - 9.5^\circ$), low ($9.5^\circ - 22.5^\circ$), medium ($22.5^\circ - 37^\circ$) and steep ($> 37^\circ$);
- the roof geometry classes are: flat, gable, hip and shed;
- facade material was grouped into brick, cement block, concrete, glass, metal, plaster, plastic, stone, and wood;
- the occupancy classes are the following: agriculture, commercial, industrial, mercantile, public, and residential.

Our dataset consists of 6477 training and 3197 testing building scenes, split by stratified sampling. The total number of street-view images is 29350 in the training dataset and 10402 in the testing dataset. Most street-view photos are of size 640×640 , but around 25% of them are taller. This is because we extended some of the images upwards – by stitching together multiple photos – to obtain a better view of taller structures. The size of the top-view image (one per building) depends on the building size.

In summary, our dataset includes the following: top-view images, street-view images, the location, direction and field of view of the street-view images, and the georeferenced footprint of the building.

In Figure 1 we present a full example, showing all images and metadata available for a single building, along with the correct output classes.

In Appendix C, we present more information about the dataset: an example of each class for each attribute, a sample of full scenes with descriptions, and a comparison with existing datasets from the literature.

4 Multi-view multi-task approach

We start by introducing the basic definitions and then present increasingly strong models for building attribute classification.

We denote the top-view image by Im_0 , and the n -th street-view input image by Im_n , for $n \in \{1, \dots, N\}$, where N is the total number of street-view images for the given building. We transform the input images to obtain spatial feature maps f_0, f_1, \dots, f_N using feature extractor networks CNN_{TV} (top-view) and CNN_{SV} (street-view), with d output channels for street-view features and d_0 output channels for top-view features:

$$f_0 = CNN_{TV}(Im_0) \quad f_n = CNN_{SV}(Im_n). \quad (1)$$

Feature vectors obtained from these feature maps by mean-pooling along spatial dimensions are denoted as v_0, \dots, v_N . We use six linear heads with softmax activation to generate the class probabilities for each of the tasks. We train the models to minimize the total cross-entropy loss summed over all of the classification tasks. We consider the following baselines.

Top-view (TV) Only the top-view input image is used. The input to the six task-specific classification layers is v_0 .

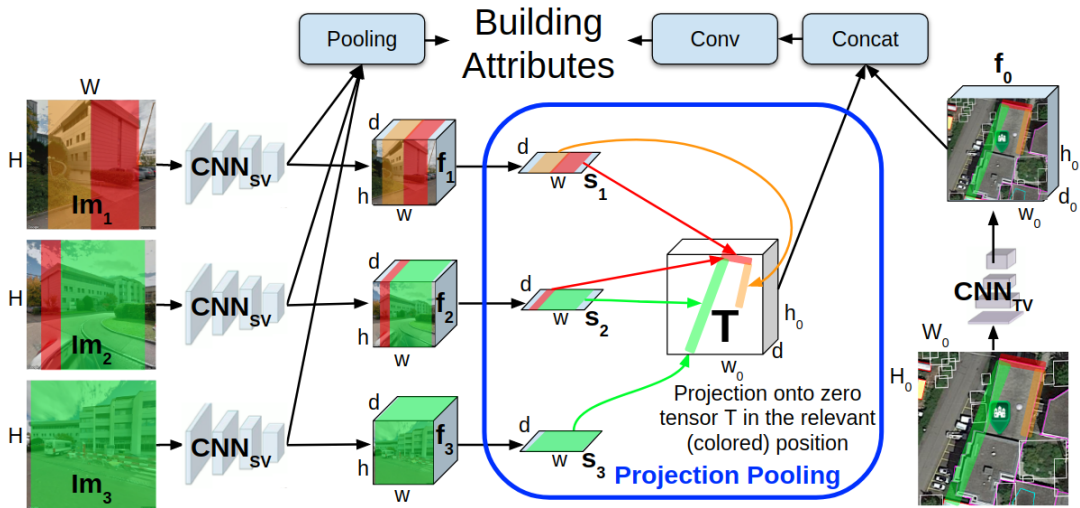


Figure 2: Our model with the projection pooling layer. The colors represent different building walls. The red and green wall features come from two different street-view images, while the orange one only from a single photo. The orange segment covers only the visible part of the building wall, as the rest of it is not visible on any street-view image. To overlap them in the top-view projection, we average the street-view features across the height dimension. We project the street-view (side walls) features onto a zero tensor (white). Then, we concatenate the projected features with the top-view feature map to form a unified representation. We further apply convolutions on top of it and concatenate with street-view features to obtain features for the final recognition.

Street-view (SV) To fuse the street-view input images, we compute feature vectors v_1, \dots, v_N , and use their average as input to the task-specific classification layers.

Street-view + Top-view separately (SV+TV separately) The different tasks achieve varying results depending on which kinds of images are given as input: street-view or top-view. Based on the results of the baselines that use a single input type (either street-view or top-view), we choose the best baseline model for each task separately. We train the top-view model to classify the roof slope and roof geometry, while the street-view model to classify other attributes. The two networks are completely separate and are trained separately.

Street-view + Top-view (SV+TV) We use two independent feature extractors: one for street-view and one for top-view images. The vectors v_1, \dots, v_N are averaged as in the street-view baseline, and then this average is concatenated with v_0 to form the input to the task-specific classification layers. This fusion is shown visually in Appendix D. We also consider a modification where the same feature extractor network is used both for the top-view and street-view images (i.e. $\text{CNN}_{\text{TV}} = \text{CNN}_{\text{SV}}$).

5 Our model

The models described in Section 4 take into account neither the relatively simple cuboid-like geometry of a typical building nor the source positions of the street-view images. These factors, especially the distance between the building and the source of the street-view photo, may impact what is visible on the input image. We design a fusion strategy to leverage the building geometry, street-view photo location, and its direction. It results in a single, unified, top-view repre-

sentation of the building. We extract the feature maps from all street-view photos as defined in Equation (1), and map these features (we call it a *projection* in this work) onto relevant parts of the building polygon, as seen on the top-view image. Those projected features are overlapped and concatenated with the top-view aerial representation to let the model infer the entire scene.

The final representation encompasses the following information: all street-view images, top-view image, building footprint, street-view image positions, directions, and fields of view.

5.1 Projection Pooling

We describe the construction of the unified building representation following the explanatory Figure 2. For each street-view image Im_i of size $[H_i, W_i, 3]$, we extract the feature map f_i of shape $[h_i, w_i, d]$, and average out the vertical dimension, while keeping the horizontal dimension intact. It results in a feature stripe s_i of shape $[w_i, d]$, which will be projected onto the building outline. Since all the street-view images in our dataset are of the same width, we can replace the w_i 's by one value w , so all the stripes s_i are in fact of shape $[w, d]$. We initialize a zero tensor T of shape $[h_0, w_0, d]$, where h_0 and w_0 are the height and width of the feature map f_0 . T represents a top-view 2D-grid of d -dimensional neurons. Neurons in T are projected from each stripe s_i . By concatenating T of shape $[h_0, w_0, d]$ with the top-view feature map f_0 of shape $[h_0, w_0, d_0]$, we construct the final unified representation.

In this paragraph, we explain the details of how we project a stripe s_i onto the tensor T . Using the building outline, source location, and direction of street-view image Im_i , we

compute the visible parts of the building polygon (represented by colored segments on tensor T in Figure 2). An efficient way of computing them is described in Appendix E. These segments correspond to parts of the edges of the building polygon visible in Im_0 . They can be discretized and approximated by a set P_i of d -dimensional neurons located in $[h_0, w_0]$ 2D-grid of T . For each neuron $p = (x_p, y_p) \in P_i$, we compute the angle at which it can be seen from the location of Im_i . This forms its cone of visibility, as presented in Figure 3. This cone lets us compute the visible part of the building corresponding to p in the image Im_i . This translates to an angle range (a_l, a_r) along the width dimension of s_i . We project the features from this range in s_i onto the (x_p, y_p) position in T . In Subsection 5.2, we explore various ways of sampling the features from a single stripe s_i . Some of the neurons in T might not be visible on any of the street-view images, or do not belong to the building polygon - the corresponding feature vectors in T will be zero vectors. If a single neuron in T gets features projected from multiple stripes, these feature vectors are max-pooled.

This description can be formulated as follows:

$$s_i[w', d'] = \frac{\sum_{h' \in [0 \dots h_i - 1]} f_i[h', w', d']}{h_i}$$

$$T[h', w'] = \max_{i \in [1 \dots N]} \text{Pool}(h', w', prt, s_i, src_i, dir_i, FoV_i)$$

Algorithm 1 $\text{Pool}(h', w', prt, s_i, src_i, dir_i, FoV_i)$

```

p = (h', w')
if p not in ConeOfVisibility(src_i, dir_i, FoV_i) then
  return 0
end if
if p not in Boundary(prt) then
  return 0
end if
if p in OccludedByOtherWall(prt, src_i, dir_i, FoV_i) then
  return 0
end if
a_l, a_c, a_r = PixelToStripeRange(p, prt, src_i, dir_i, FoV_i)
return StripeSample(a_l, a_c, a_r, w, s_i, FoV_i)

```

Where h', w', d' are indexes of height, width and depth dimensions, prt is the building footprint, N is number of street-view images, src_i is source location of i -th street-view image, dir_i is direction of i -th street-view image and FoV_i is its field of view.

5.2 Stripe sampling (SS)

A single neuron in the top-view feature map can correspond to a relatively large area in the original input image. The angle of visibility for a neuron on a street-view image can cover multiple pixels in s_i , especially for the close-by photos (see the red area in Figure 3). For example, a 1×1 pixel in the output feature map of ResNet-50 (He et al. 2016) with a total stride of 32 corresponds to an area of 32×32 pixels in the input image. The details on how to calculate the neuron value can be crucial for the overall performance of the

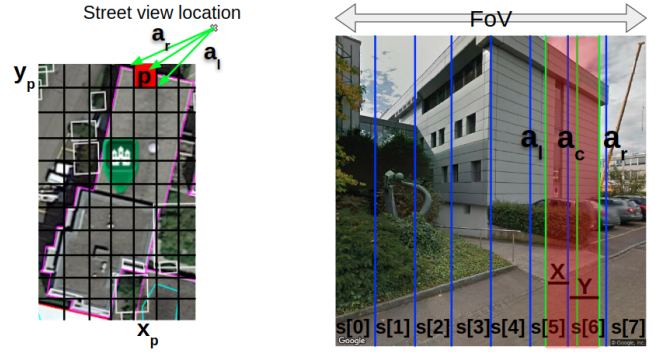


Figure 3: Different strategies for sampling stripe features in the projection pooling layer. The red box represents a neuron in 2D-grid T . The green rays towards the neuron center and its sides are also marked as green vertical lines on the street-view image. s is defined as the average along the height dimension of street-view features. In this example, we assume $w = 8$. The 'nearest' strategy takes the nearest position in the stripe i.e. $s[6]$. The 'sum' strategy takes the weighted sum between pixel boundaries $Xs[5] + Ys[6]$. The 'avg' normalizes the 'sum' strategy i.e. $(Xs[5] + Ys[6]) / (X + Y)$.

model (He et al. 2017). We define three different strategies for deriving the neuron value from the s_i stripes. While we describe these strategies below, we also presented them visually in Figure 3. In all strategies, FoV represents the field of view angle for the entire street-view image, w is the width of the associated stripe s , and $a'_x = w \frac{a_x}{FoV}$ for $x \in \{l, r, c\}$.

Nearest (N) uses the angle, measured clockwise, between the beginning of the field of view of given street-view image and the center of the neuron. We denote this angle by a_c . In this strategy, we use a single feature vector from s to calculate the value of neuron p :

$$p_{\text{nearest}} = s(\lfloor a'_c \rfloor). \quad (2)$$

In other words, we draw a ray from the location of the street-view photo towards the neuron's center, calculate the position $p \in \{0, \dots, w - 1\}$ of its intersection with the stripe s , and take the d -dimensional feature vector at this position (recall that s is of shape $[w, d]$).

Sum (S) uses two rays pointing towards the pixel's ends instead of one ray pointing towards the pixel's center. Denote the angles of these rays by a_l and a_r for the left and right one, respectively. Then, the value of the projected feature vector is defined below, where $\{x\} = x - \lfloor x \rfloor$.

$$p_{\text{sum}} = s(\lfloor a'_l \rfloor) \cdot \{ -a'_l \} + s(\lfloor a'_r \rfloor) \cdot \{ a'_r \} + \sum_{i=\lceil a'_l \rceil}^{\lfloor a'_r \rfloor - 1} s(i) \quad (3)$$

Average (A) follows a similar strategy to Sum - i.e. it takes into account feature vectors from multiple positions along the feature stripe s . However, a potential problem with the Sum strategy is that the magnitude of values in the resulting vector may vary significantly with the distance to the building wall: more feature vectors are summed if the building wall is in proximity. Therefore, we propose a variant of

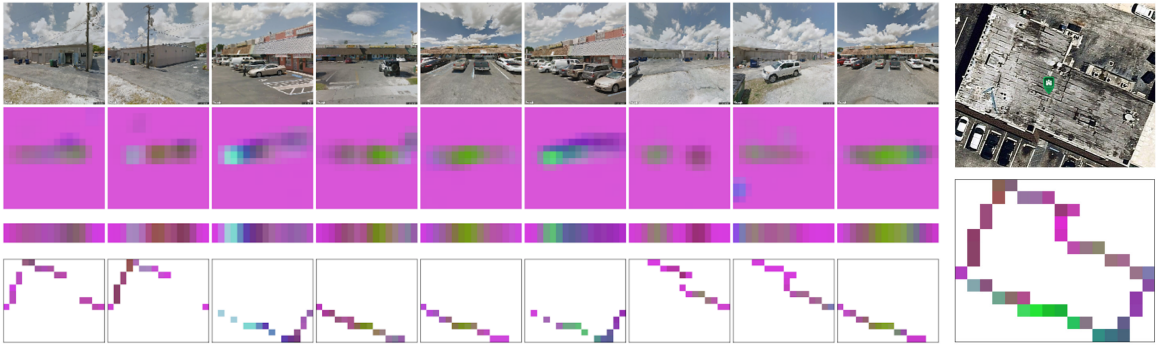


Figure 4: Left: We show street-view photos corresponding to a single building (top row), visualization of the extracted feature maps f_i before averaging out the height dimension (second row), and after (third row). In the last row, we show features contributed to specific neurons of the unified representation. Right: Visualization of the unified representation pooled from all the images. The neurons shown as white did not get any features projected onto them, i.e., their values are 0. For a larger version of this figure, see Appendix F.

the Sum strategy, where the output is additionally normalized. We choose to simply divide the resulting feature vector by the width of the part of s corresponding to the neuron p :

$$p_{\text{average}} = \frac{p_{\text{sum}}}{a'_r - a'_l} \quad (4)$$

5.3 Visualizing projected features

We visualize the features extracted from the street-view photos and how they are projected to create the final unified building representation. We obtain features from the test set pictures corresponding to multiple buildings and project them to three dimensions using principal component analysis, resulting in RGB coordinates. It allows us to visualize a single feature vector as a color.

We visualize the street-view feature maps both before and after their height dimension is averaged out. Then, we look at the feature vectors projected onto the building polygon from each street-view photo separately. We show this in Figure 4. Note that the south wall looks substantially different from the others for the selected building, and this difference can be seen in the visualizations. Moreover, feature maps in positions where no structure is visible get projected to the same uniform color (pink), showing that the feature extractor ignores irrelevant information. Finally, we examine the unified representation vectors, i.e., after max-pooling the features projected from different views. Again, we see that the side of the building providing different visual information has a substantially different projection.

6 Experiments and results

6.1 Experimental setup

We benchmark our approach on the newly collected dataset of building attributes, as defined in Section 3. Street-view images are resized to size 500×500 . The top-view image is cropped to the bounding box containing the building of interest and resized to keep the aspect ratio so that the length of the longer side is 500. As the feature extractor network, we use the ResNet-50 model pre-trained on the ImageNet

dataset, as available in PyTorch (Paszke et al. 2017). We discard the final fully connected output layer. We freeze the parameters of the stem and the first block in the pre-trained ResNet-50 feature extractors and do not fine-tune the batch normalization layers. We train the network using stochastic gradient descent with momentum, on a single GPU (see Appendix G for details), and with a batch size of one building. The effective number of images in a single batch is equal to 1 for the top-view branch, while for the street-view branch, it varies from 1 to 9. We use the learning rate of 0.0001 for ten epochs and then 0.00001 for one more epoch. We set the momentum to 0.9. We apply L2 regularization with a weight decay of 0.001 and augment the dataset with random color jittering. We compare the models using average classification accuracy over the six tasks. For details about hyperparameter tuning, see Appendix H.

Image dropout (ID) Inspired by dropout (Srivastava et al. 2014), we regularize the training by randomly dropping entire street-view images, which we call *image dropout*. During training, every street-view image in the batch of a given building is omitted with probability p . We make sure that there is always at least one street-view image in a batch. We do not rescale the values of the features as done in the original dropout. With image dropout, we force the model to use a different set of images in each iteration. We do not apply image dropout at test time, allowing the model to use all of the street-view images available for the given building.

Projection thickness (TH) When rounding up the top-view building polygon to a set of neurons in T , we obtain a thin building outline, where each side is discretized as a one-pixel wide line. We consider using an outline wider than one. Projection thickness of k means that the building outline is discretized to line segments, which are k neurons wide. We assume that pixels belonging to the same side do not occlude each other. Widening the polygon makes it easier for the convolutional layer applied on top of the unified representation to capture features from adjacent walls.

Cutout (CU) To further regularize the training over multiple potentially redundant street-view images, we apply

Model	Testing Accuracy						
	Constr	#Floors	Roof Pitch	Roof Geom	Facade Material	Occup	Avg
TV - only top-view	72.2	57.2	79.2	90.9	51.1	70.0	70.10
SV - only street-view	73.4	72.2	76.7	87.0	61.5	74.2	74.14
SV+TV, $\text{CNN}_{\text{TV}} = \text{CNN}_{\text{SV}}$	73.1	72.0	79.7	91.1	58.5	72.5	74.49
SV+TV	73.0	72.7	79.4	91.4	57.9	73.2	74.59
SV+TV, separately	73.3	72.5	77.7	89.8	60.3	74.2	74.64
Projection pooling	76.0	75.6	81.3	91.9	62.4	76.6	77.28

Table 1: The classification accuracy results of our method and the baselines.

Cutout (DeVries and Taylor 2017). For every street-view image, with probability q , we blackout 40% of pixels, by covering the image with a randomly placed black rectangle. Using this approach, we force the model to rely on multiple parts of an image when performing classification.

Splitting the street-view images (SS) To perform projection pooling, we average the street-view feature maps f_i along the height dimension, which gives a rough feature stripe s_i . We also investigate a different strategy, which allows the model to take into account the differences between lower, middle, and upper parts of the street-view images. We split the feature representation into k different tensors along the height dimension, and concatenate them along the depth dimension. In other words, we shift the height dimension into the depth dimension. From a feature map f_i of size $[h, w, d]$, we obtain one of size $[\frac{h}{k}, w, d \cdot k]$ and apply mean-pooling along height dimension with projection pooling.

6.2 Results

In this subsection, we discuss the experimental results.

In Table 1, we present a comparison between competitive methods and the new proposed model with the projection pooling layer. Using only the top-view images gives worse results than using only the street-view photos. It is still better than one would expect, given that most parts of the building are not visible on the top-view image. Unsurprisingly, using the street-view rather than the top-view gives the most substantial gains when counting the number of floors (+15%) and predicting facade material (+10.4%). On the other hand, top-view images are more informative when it comes to roof geometry (+3.9%) and roof pitch (+2.5%).

Combining both top-view and street-view images gives better results than using a single source, but only by 0.35% than when using street-view alone. Separate networks for the top and street-view images yield a small improvement. We obtain the best baseline results when training the top-view and street-view networks independently on different tasks.

Incorporating the projection pooling layer results in about 3% accuracy improvement over the best baseline.

In Appendix I, we present the results of an ablation study, which examines the impact of all components of our final model. First, we train a vanilla projection pooling model with different stripe sampling strategies, and find that using the averaging strategy gives the best results (75.93%). Adding image dropout with probability $p = 50\%$ further regularizes the model, and increases average accuracy

(+0.23%). We then tested values higher than 1 for projection thickness, and found that using 3 improves performance (+0.38%), while increasing beyond this number did not bring further gains. Applying cutout with probability $q = 50\%$ improves our model even further (+0.33%), which shows the importance of using a wide variety of regularization techniques. The final improvement (+0.41%) comes from splitting the street-view feature maps into three tensors, and concatenating them along the depth dimension, as described in Subsection 6.1. In this way, lower, middle, and upper parts of the building are separately projected, which is especially helpful for discrimination of the number of floors.

Impact of multiple images We investigate the impact of varying the number of street-view images per building. For $k \in \{1, 2, 3, 4\}$, we test our best model with a restriction to use at most k street-view images.

The results of this comparison are shown in Appendix J. We see a substantial (+1.36%) gain from using more than one street-view image, suggesting that photos from multiple angles are often necessary for correct classification. On the other hand, the benefits of adding more street-view images quickly plateau, as there is a considerable overlap of information provided by the different street-view photos.

7 Conclusions

Our study presents a novel solution to a practical problem of building understanding. For the first time, this problem is approached using the building geometry inside a deep neural architecture to create a unified high-dimensional representation. We propose a new way to integrate the features from multiple views called *projection pooling*. It is a general method for creating a unified representation of 3D objects from orthogonal projections and is particularly well suited for building analysis. In the future, it can be tested against analogical setups, such as mammogram analysis (Morrell et al. 2018). We propose a model for building feature recognition, which incorporates the projection pooling layer, and its results are superior to highly tuned baseline models.

We build a new dataset with fine-grained building attributes and analyze techniques for integrating information from multiple views. The dataset establishes a demanding benchmark for state-of-the-art deep learning methods. It requires reasoning about numerous images at once to give accurate results. We plan to expand the dataset to detect objects, such as doors and windows.

References

- Andersson, V. O.; Birck, M. A.; and Araujo, R. M. 2017. Investigating crime rate prediction using street-level images and siamese convolutional neural networks. In *Latin American Workshop on Computational Neuroscience*.
- Armagan, A.; Hirzer, M.; Roth, P. M.; and Lepetit, V. 2017a. Accurate camera registration in urban environments using high-level feature matching. In *Proceedings of the British Machine Vision Conference*.
- Armagan, A.; Hirzer, M.; Roth, P. M.; and Lepetit, V. 2017b. Learning to align semantic segmentation and 2.5 d maps for geolocalization. In *Proceedings of the IEEE Conference on Computer Vision and Pattern Recognition*, 3425–3432.
- Bódis-Szomorú, A.; Riemenschneider, H.; and Van Gool, L. 2016. Efficient volumetric fusion of airborne and street-side data for urban reconstruction. In *International Conference on Pattern Recognition*, 3204–3209. IEEE.
- Cao, R.; Zhu, J.; Tu, W.; Li, Q.; Cao, J.; Liu, B.; Zhang, Q.; and Qiu, G. 2018. Integrating Aerial and Street View Images for Urban Land Use Classification. *Remote Sensing*.
- Chu, H.; Wang, S.; Urtasun, R.; and Fidler, S. 2016. Housecraft: Building houses from rental Ads and street views. In *Proceedings of the European Conference on Computer Vision*, 500–516. Springer.
- Cohen, A.; Oswald, M. R.; Liu, Y.; and Pollefeys, M. 2017. Symmetry-Aware façade parsing with occlusions. In *2017 International Conference on 3D Vision (3DV)*.
- Cordts, M.; Omran, M.; Ramos, S.; Rehfeld, T.; Enzweiler, M.; Benenson, R.; Franke, U.; Roth, S.; and Schiele, B. 2016. The cityscapes dataset for semantic urban scene understanding. In *Proceedings of the IEEE Conference on Computer Vision and Pattern Recognition*, 3213–3223.
- DeVries, T.; and Taylor, G. W. 2017. Improved regularization of convolutional neural networks with cutout. *arXiv preprint arXiv:1708.04552*.
- Dubey, A.; Naik, N.; Parikh, D.; Raskar, R.; and Hidalgo, C. A. 2016. Deep learning the city: Quantifying urban perception at a global scale. In *Proceedings of the European Conference on Computer Vision*, 196–212. Springer.
- Gadde, R.; Jampani, V.; Marlet, R.; and Gehler, P. V. 2017. Efficient 2D and 3D facade segmentation using auto-context. *IEEE Transactions on Pattern Analysis and Machine Intelligence (PAMI)* 40(5): 1273–1280.
- Gebri, T.; Krause, J.; Wang, Y.; Chen, D.; Deng, J.; Aiden, E. L.; and Fei-Fei, L. 2017a. Using deep learning and Google Street View to estimate the demographic makeup of neighborhoods across the United States. *Proceedings of the National Academy of Sciences* 114(50): 13108–13113.
- Gebri, T.; Krause, J.; Wang, Y.; Chen, D.; Deng, J.; and Fei-Fei, L. 2017b. Fine-grained car detection for visual census estimation. In *Thirty-First AAAI Conference on Artificial Intelligence*.
- He, K.; Gkioxari, G.; Dollár, P.; and Girshick, R. B. 2017. Mask R-CNN. In *Proceedings of the IEEE International Conference on Computer Vision*, 2961–2969.
- He, K.; Zhang, X.; Ren, S.; and Sun, J. 2016. Deep Residual Learning for Image Recognition. In *Proceedings of the IEEE Conference on Computer Vision and Pattern Recognition*.
- Hirzer, M.; Arth, C.; Roth, P. M.; and Lepetit, V. 2017. Efficient 3D Tracking in Urban Environments with Semantic Segmentation. In *Proceedings of the British Machine Vision Conference*.
- Hoffmann, E. J.; Wang, Y.; Werner, M.; Kang, J.; and Zhu, X. X. 2019. Model Fusion for Building Type Classification from Aerial and Street View Images. *Remote Sensing*.
- Hu, S.; Feng, M.; Nguyen, R. M.; and Hee Lee, G. 2018. CVM-Net: Cross-View Matching Network for Image-Based Ground-to-Aerial Geo-Localization. In *Proceedings of the IEEE Conference on Computer Vision and Pattern Recognition*, 7258–7267.
- Kang, J.; Körner, M.; Wang, Y.; Taubenböck, H.; and Zhu, X. X. 2018. Building instance classification using street view images. *ISPRS Journal of Photogrammetry and Remote Sensing*.
- Koch, D.; Despotovic, M.; Sakeena, M.; Döllner, M.; and Zeppelzauer, M. 2018. Visual estimation of building condition with patch-level convnets. In *Proceedings of the 2018 ACM Workshop on Multimedia for Real Estate Tech*, 12–17. ACM.
- Kozinski, M.; Gadde, R.; Zagoruyko, S.; Obozinski, G.; and Marlet, R. 2015. A MRF shape prior for facade parsing with occlusions. In *Proceedings of the IEEE Conference on Computer Vision and Pattern Recognition*, 2820–2828.
- Li, Y.; Hu, Q.; Wu, M.; Liu, J.; and Wu, X. 2016. Extraction and simplification of building façade pieces from mobile laser scanner point clouds for 3d street view services. *ISPRS International Journal of Geo-Information* 5(12): 231.
- Liu, H.; Zhang, J.; Zhu, J.; and Hoi, S. C. H. 2017. DeepFacade: A Deep Learning Approach to Facade Parsing. In *Proceedings of the Twenty-Sixth International Joint Conference on Artificial Intelligence, IJCAI 2017, Melbourne, Australia, August 19-25, 2017*.
- Lotte, R.; Haala, N.; Karpina, M.; Aragão, L.; Shimabukuro, Y.; et al. 2018. 3D Façade Labeling over Complex Scenarios: A Case Study Using Convolutional Neural Network and Structure-From-Motion. *Remote Sensing*.
- Martinovic, A.; and Van Gool, L. 2013. Bayesian grammar learning for inverse procedural modeling. In *Proceedings of the IEEE Conference on Computer Vision and Pattern Recognition*, 201–208.
- Mathias, M.; Martinović, A.; and Van Gool, L. 2016. ATLAS: A three-layered approach to facade parsing. *International Journal of Computer Vision* 118(1): 22–48.
- Mitra, N. J.; Pauly, M.; Wand, M.; and Ceylan, D. 2012. Symmetry in 3D Geometry: Extraction and Applications. In *Eurographics*.
- Morrell, S.; Wojna, Z.; Khoo, C. S.; Ourselin, S.; and Iglesias, J. E. 2018. Large-Scale Mammography CAD with Deformable Conv-Nets. In *Image Analysis for Moving Organ, Breast, and Thoracic Images*, 64–72. Springer.

- Musialski, P.; Wonka, P.; Recheis, M.; Maierhofer, S.; and Purgathofer, W. 2009. Symmetry-Based Façade Repair. In *Proceedings of the Vision, Modeling, and Visualization Workshop 2009, November 16-18, 2009, Braunschweig, Germany*, 3–10.
- Paszke, A.; Gross, S.; Chintala, S.; Chanan, G.; Yang, E.; DeVito, Z.; Lin, Z.; Desmaison, A.; Antiga, L.; and Lerer, A. 2017. Automatic differentiation in PyTorch. In *NIPS-W*.
- Riemenschneider, H.; Bódis-Szomorú, A.; Weissenberg, J.; and Van Gool, L. 2014. Learning where to classify in multi-view semantic segmentation. In *Proceedings of the European Conference on Computer Vision*, 516–532. Springer.
- Riemenschneider, H.; Krispel, U.; Thaller, W.; Donoser, M.; Havemann, S.; Fellner, D.; and Bischof, H. 2012. Irregular lattices for complex shape grammar facade parsing. In *Proceedings of the IEEE Conference on Computer Vision and Pattern Recognition*, 1640–1647. IEEE.
- Roddick, T.; Kendall, A.; and Cipolla, R. 2019. Orthographic Feature Transform for Monocular 3D Object Detection. In *30th British Machine Vision Conference 2019, BMVC 2019, Cardiff, UK, September 9-12, 2019*. BMVA Press.
- Serna, A.; Marcotegui, B.; and Hernández, J. 2016. Segmentation of façades from urban 3D point clouds using geometrical and morphological attribute-based operators. *ISPRS International Journal of Geo-Information* 5(1): 6.
- Song, W.; Workman, S.; Hadzic, A.; Zhang, X.; Green, E.; Chen, M.; Souleyrette, R.; and Jacobs, N. 2018. FARSA: Fully Automated Roadway Safety Assessment. In *Winter Conference on Applications of Computer Vision (WACV)*, 521–529. IEEE.
- Srivastava, N.; Hinton, G.; Krizhevsky, A.; Sutskever, I.; and Salakhutdinov, R. 2014. Dropout: a simple way to prevent neural networks from overfitting. *The Journal of Machine Learning Research* 15(1): 1929–1958.
- Srivastava, S.; Vargas Muñoz, J. E.; Lobry, S.; and Tuia, D. 2018. Fine-grained landuse characterization using ground-based pictures: a deep learning solution based on globally available data. *International Journal of Geographical Information Science* 1–20.
- Srivastava, S.; Vargas-Muñoz, J. E.; and Tuia, D. 2019. Understanding urban landuse from the above and ground perspectives: A deep learning, multimodal solution. *Remote Sensing of Environment*.
- Stone, H. 2018. *Exposure and vulnerability for seismic risk evaluations*. Ph.D. thesis, UCL (University College London).
- Teboul, O.; Kokkinos, I.; Simon, L.; Koutsourakis, P.; and Paragios, N. 2011. Shape grammar parsing via reinforcement learning. In *Proceedings of the IEEE Conference on Computer Vision and Pattern Recognition*, 2273–2280. IEEE.
- Tyleček, R.; and Šára, R. 2013. Spatial pattern templates for recognition of objects with regular structure. In *German Conference on Pattern Recognition*, 364–374. Springer.
- Wegner, J. D.; Branson, S.; Hall, D.; Schindler, K.; and Perona, P. 2016. Cataloging public objects using aerial and street-level images-urban trees. In *Proceedings of the IEEE Conference on Computer Vision and Pattern Recognition*, 6014–6023.
- Workman, S.; Souvenir, R.; and Jacobs, N. 2015. Wide-area image geolocalization with aerial reference imagery. In *Proceedings of the IEEE International Conference on Computer Vision*, 3961–3969.
- Workman, S.; Zhai, M.; Crandall, D. J.; and Jacobs, N. 2017. A Unified Model for Near and Remote Sensing. In *Proceedings of the IEEE International Conference on Computer Vision*, 2688–2697.
- Wu, C.; Frahm, J.-M.; and Pollefeys, M. 2010. Detecting large repetitive structures with salient boundaries. In *Proceedings of the European Conference on Computer Vision*, 142–155. Springer.
- Yang, M. Y.; and Förstner, W. 2011. A hierarchical conditional random field model for labeling and classifying images of man-made scenes. In *2011 IEEE International Conference on Computer Vision Workshops (ICCV Workshops)*, 196–203. IEEE.
- Yao, Y.; Luo, Z.; Li, S.; Fang, T.; and Quan, L. 2018. Mvsnet: Depth inference for unstructured multi-view stereo. In *Proceedings of the European Conference on Computer Vision*, 767–783.
- Zeppelzauer, M.; Despotovic, M.; Sakeena, M.; Koch, D.; and Döller, M. 2018. Automatic prediction of building age from photographs. In *Proceedings of the 2018 ACM on International Conference on Multimedia Retrieval*, 126–134. ACM.
- Zhai, M.; Bessinger, Z.; Workman, S.; and Jacobs, N. 2017. Predicting ground-level scene layout from aerial imagery. In *Proceedings of the IEEE Conference on Computer Vision and Pattern Recognition*, 867–875.
- Zhang, H.; Xu, K.; Jiang, W.; Lin, J.; Cohen-Or, D.; and Chen, B. 2013. Layered analysis of irregular facades via symmetry maximization. *ACM Transactions on Graphics (TOG)* 32(4): 121–1.
- Zhu, Y.; Deng, X.; and Newsam, S. 2019. Fine-grained land use classification at the city scale using ground-level images. *IEEE Transactions on Multimedia*.

A Building location heatmap

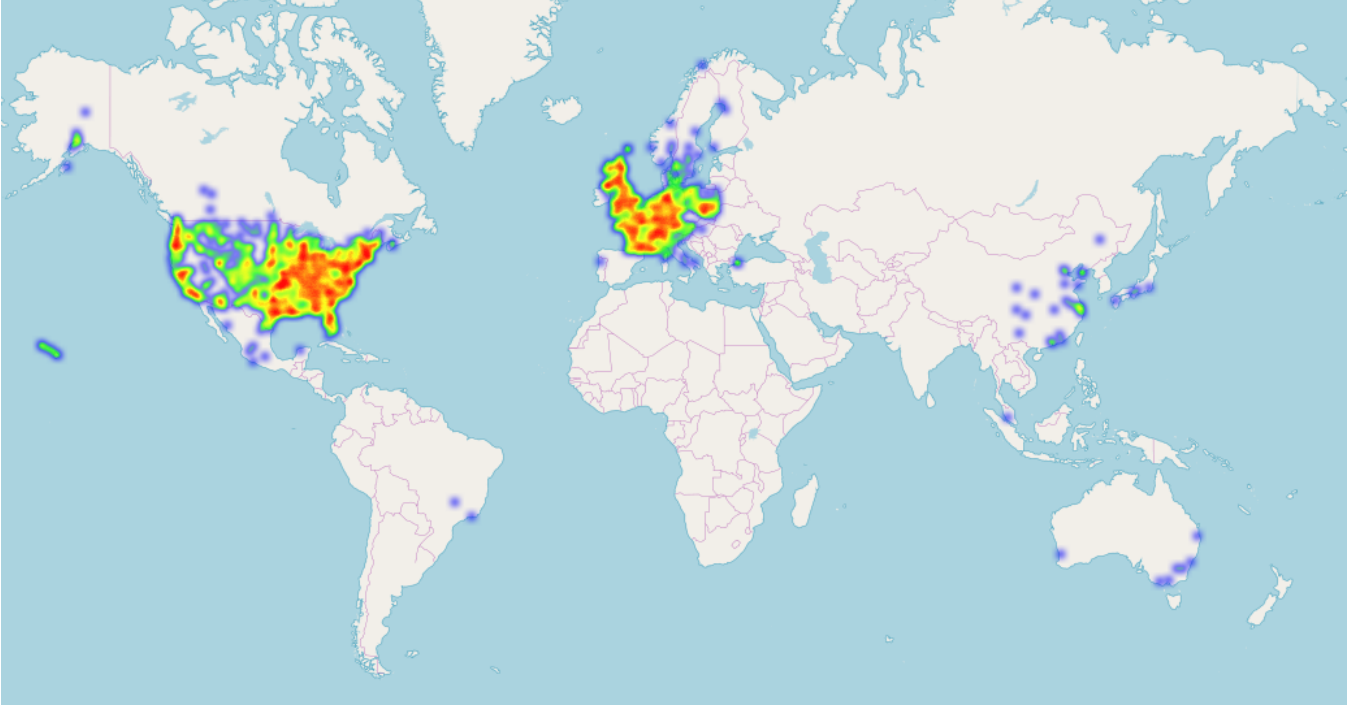


Figure 1: A world heatmap of the building locations for our dataset. Our dataset represents a broad variety of buildings and architectural styles.

B Resolution of the top-view imagery

Aerial photos' spatial resolution depends on the latitude and can be expressed as *zoom* 19 using the *slippy map* definition. The exact spatial resolution r , measured in meters per pixel, is expressed by the following formula:

$$r = \text{equator length} \cdot \cos(\text{latitude}) \cdot \frac{1}{2^{19}} \cdot \frac{1}{2^8}.$$

The factor of 2^{-19} corresponds to the zoom, whereas the factor of 2^{-8} matches with the square tile size of 256 pixels.

C Dataset details

In this section, we provide more dataset examples, as well as a comparison with existing datasets from the literature.

In Table 1, we show one instance of every class for every attribute. In Figures 2-7, we show challenging scenes from our dataset, together with descriptions explaining how correct classification is still possible. Finally, in Table 2 we compare our dataset with existing datasets in the same domain.

Construction type	 Concrete (5071)	 Masonry (2230)	 Wood (1195)	 Metal (1036)		
Roof pitch	 Flat (5382)	 Low (1849)	 Moderate (2232)	 High (214)		
Roof geometry	 Flat (4933)	 Gable (1532)	 Hip (553)	 Shed (74)		
Occupancy type	 Agriculture (89)	 Commercial (4224)	 Industrial (714)	 Mercantile (253)	 Public (389)	 Residential (2475)
Number of floors	 1 (4438)	 2 (2864)	 3 (873)	 4 (390)	 5 or more (1067)	
Facade material	 Brick (1274)	 Cement block (403)	 Concrete (1182)	 Glass (86)	 Metal (829)	
	 Plaster (3253)	 Plastic (359)	 Stone (119)	 Wood (133)		

Table 1: Examples of street-view images for every class in the dataset together with the building counter for that class in the training dataset. The dataset presents many challenges, such as occlusions and small object recognition from afar. Some images contain multiple buildings, confusing the model, and a few of them even miss the correct building.



Figure 2: Photos of a shopping mall from completely different perspectives. The model sees three different sides of the building from different angles and must be able to filter out the cars appearing in images.



Figure 3: A typical example from an urban area, where more than one building is visible on the photo. Moreover, it is not ideally cropped in the second image. Observe that the roof pitch could be correctly estimated only from the third photo.

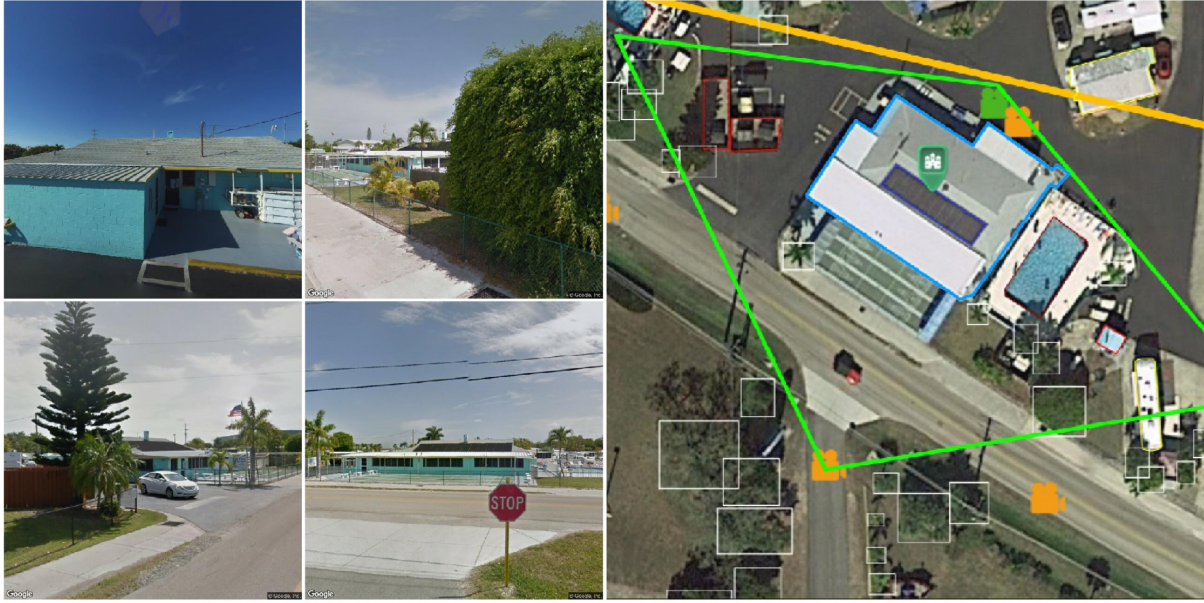


Figure 4: Different photos of the same building highlighting various difficulties of the dataset. The first image is from a very close distance. The second image is partially occluded; the third one is also occluded by a visible car. The last one is from afar. Note that we can infer the construction type only from the first photo, where the bricks can be seen, whereas the last photo clearly shows the number of stories.

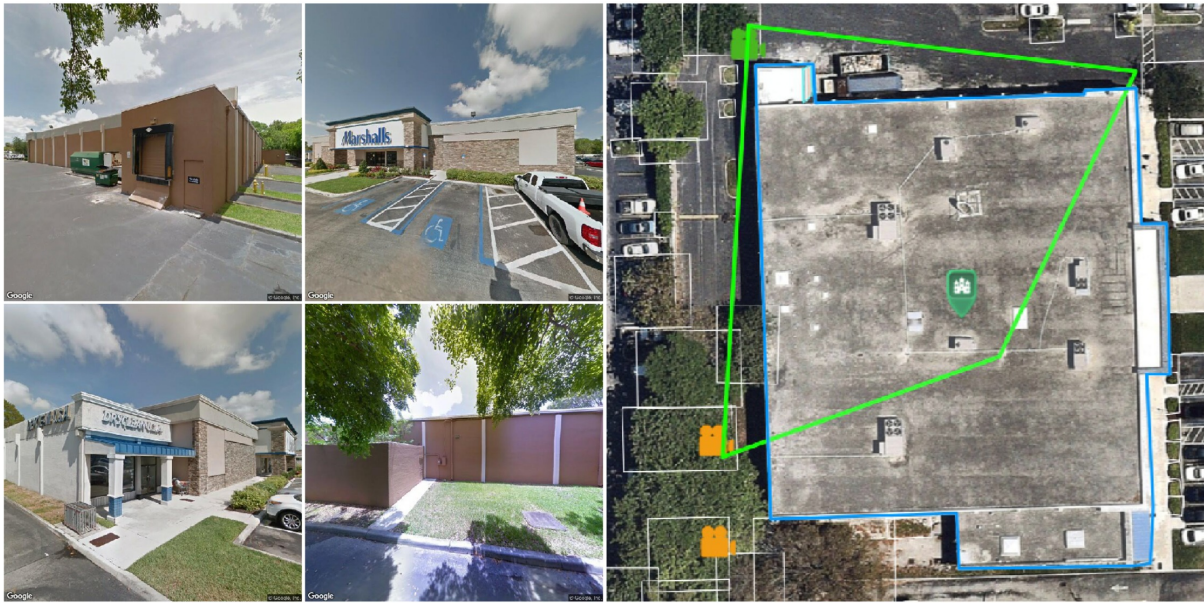


Figure 5: Four different photos of the same building. They all look like different buildings. The last image is partially occluded. The facade on the second and third photo might suggest the building is made of masonry, when the correct answer is reinforced concrete.



Figure 6: A building which is almost completely occluded but we are still able to infer some of its features. It has one floor, low roof pitch and is made of wood.



Figure 7: A challenging example, where the building is occluded on the first photo, and partially occluded on the second one with cars present. Moreover, we can infer the number of floors only from the last photo, since the building is not fully visible in the third one. The photos are from different sides of the building, making the task even more difficult.

Table 2: Comparison of datasets related to building analysis. #SV - number of street-view images, #TV - number of top-view images.

Dataset	#SV	#TV	Location	Dataset Type	Multi-view
ICG Graz50 [10]	50		Graz (Austria)	2D Segmentation	✗
eTRIMS [7]	60		Multiple	2D Segmentation	✗
ENPC ArtDeco [5]	79		Paris (France)	2D Segmentation	✗
ECP Hausmannian [12]	104		Paris (France)	2D Segmentation	✗
CMP [13]	378		Multiple	2D Segmentation	✗
LabelMeFacade [4]	945		Multiple	2D Segmentation	✗
ZuBuD [11]	1 005		Zurich (Switzerland)	2D Segmentation	✗
RueMonge2014 [9]	428		France	2D & 3D Segmentation	✓
SJC [8]	175		Brazil	2D & 3D Segmentation	✓
Limmatquai and Munsterhof [3]	1 476	23	Zurich (Switzerland)	3D Reconstruction	✓
CVUSA [14]	1 588 655	879 318	USA	Geolocalization	✓
Kang et al. [6]	19 658		USA, Canada	Classification (occupancy type)	✗
UC Merced [16]		2 100	USA	Classification (land use)	✗
DeepSat [2]		950 000	Global	Classification (land use)	✗
Albert et al [1]		140 000	Europe	Classification (land use)	✗
Brooklyn and Queens [15]	38 603	10 044	NYC (USA)	Classification (3 attributes)	✓
Ours	39 752	9 674	Global	Classification (6 attributes)	✓

D Baseline fusion

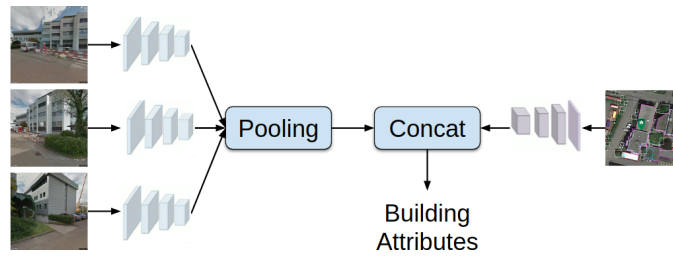


Figure 8: We average the street-view features and then concatenate them with top-view features for the final class prediction.

E Computing the visible parts of the building

For each street-view image we compute which part of the top-view building polygon is visible. Note that many real-life building outlines are non-convex, and so the visible part might be a disconnected set of pieces of sides of the building polygon. We also take into account the occlusions caused by adjacent buildings. Here, we describe the approaches we investigated, comparing their time complexities in terms of the number of sides of the polygon n .

First, let us describe a naive approach that works in $O(n^2)$. We begin by fixing a single side, and computing what part of it is visible (possibly the entire side is occluded, in which case it will be ignored). To check visibility, we simply iterate through all the remaining sides, checking for occlusions.

In practice, we noticed that using a naive $O(n^2)$ algorithm was considerably slowing down both training and inference. This is because the number of polygon vertices – and thus sides – in our dataset can be quite large. In particular, one can often find multiple vertices near the building corners, due to post-processing of human annotations for loop closing. Therefore, we also developed a faster sweep line-based algorithm, which works in $O(n \log n)$ time.

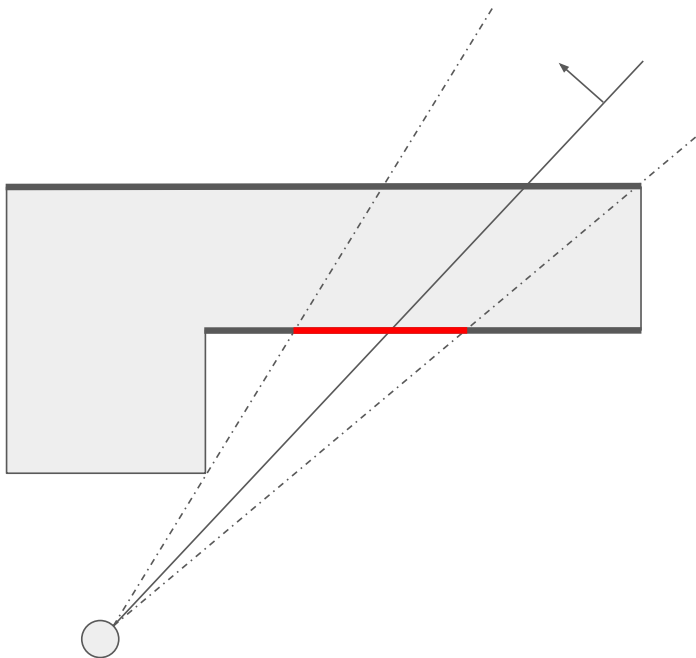


Figure 9: Visualization of the radial sweep algorithm. We denote a single position of the ray with a solid line, where the arrow shows the direction of movement. The last and next events are denoted with dotted lines. The current set S contains the two bolded sides of the building polygon, and the bottom one is visible. In red we show the visible side limited to the current range of ray angles, which will be included in the final result. When we process the next event, two more sides will be added to S , and the visible building side will change.

The sweep line algorithm works as follows. We start with a ray originating at the street-view image location and pointing in an arbitrary direction, and rotate the ray until it makes a complete turn. Intuitively, any moment when the ray intersects the building polygon corresponds to some part of the building being visible, and the visible part is the closest intersection point of the ray with the building polygon. At any point during the sweep, we maintain the set S of all polygon sides intersected by the ray. Each side needs to be inserted into S exactly once during the sweep, and then (at a later point) deleted. Therefore, even though the radial sweep is a continuous process, there are only $2n$ events (each corresponding to a specific angle of the ray) that change the contents of S . Note that the polygon part visible at a given moment corresponds to a side in S which intersects the ray closest to the origin, and this does not change as long as the set S does not change. Thus, between every two consecutive events, we need to look up the closest segment in S , and add a part of this segment to the final result. The segment of interest can be extracted from S in $O(\log n)$ time, assuming S is implemented as a balanced Binary Search Tree, where the elements (polygon sides) are sorted according to their intersection with the ray. Thus, the complexity of the entire algorithm is indeed $O(n \log n)$. In Figure 9 we show a single moment during the radial sweep.

F Projection pooling visualizations

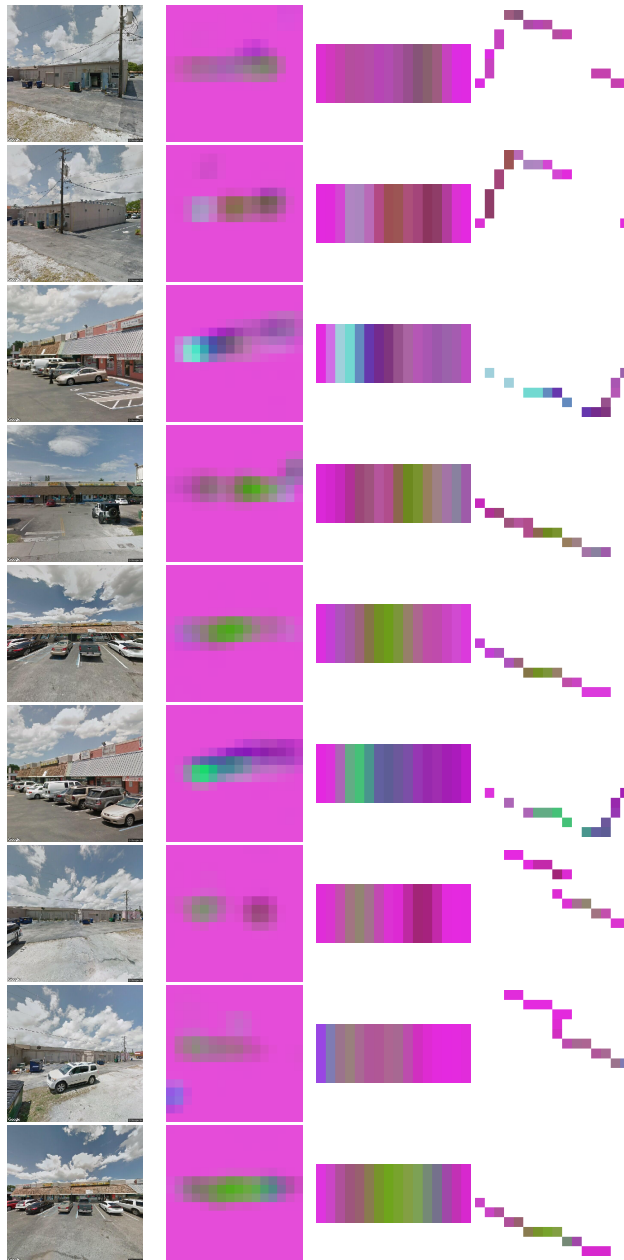


Figure 10: Larger version of projection pooling visualization. Each row corresponds to one street-view image.

G Infrastructure and frameworks

We trained all our models on a Linux machine with a single GeForce GTX 1080 Ti GPU. To build our networks we used PyTorch 1.4.

H Hyperparameter tuning

Here we report the hyperparameter settings that were considered during the development of our models. We sequentially varied each of the different hyperparameters in the order reported in Table 3.

Hyperparameter	Values tried
Fine tune batch norm	{ No , Yes}
Crop top-view to building	{No, Yes }
Number of frozen ResNet blocks	{0, 1, 2 , 3, 4}
ResNet type	{ResNet-34, ResNet-50 }
Initial learning rate	{1e-5, 3e-5, 1e-4 , 3e-4, 1e-3, 1e-2}
Weight decay	{0.0, 1e-4, 1e-3 , 1e-2}
Image augmentation	{None, Color jittering , Random grayscale}
Stipe sampling strategy	{Nearest, Sum, Average }
Image dropout probability	{0.0, 0.2, 0.4, 0.5 , 0.8, 0.9}
Projection thickness	{1, 2, 3 , 4}
Cutout probability	{0.0, 0.5 , 1.0}
Number of street-view splits	{1, 2, 3 , 4, 5}

Table 3: Values tried for each of the hyperparameters. Final selected value shown in bold.

I Ablation study

Testing Accuracy											
SS	ID	TH	CU	SS	Constr	#Floors	Roof Pitch	Roof Geom	Facade Material	Occup	Avg
N	0	1	0	1	76	73.6	78.9	91.3	59.5	75.2	75.76
S	0	1	0	1	75.7	73.3	79	91.5	59.5	75.7	75.78
A	0	1	0	1	76.1	73.5	78.7	91.6	60	75.7	75.93
A	0.5	1	0	1	75.9	73.1	80	91.8	60.2	75.8	76.16
A	0.5	3	0	1	76.4	74	80.2	91.5	60.8	76.4	76.54
A	0.5	3	0.5	1	76.3	73.5	80.5	92.1	62.3	76.5	76.87
A	0.5	3	0.5	3	76	75.6	81.3	91.9	62.4	76.6	77.28

Table 4: Ablation experiments for the model with projection pooling layer. SS - stripe sampling; ID - image dropout; TH - projection thickness; CU - cutout probability; SS - number of vertical splits for street-view images.

J Impact of multiple images

Testing Accuracy							
	Constr	#Floors	Roof Pitch	Roof Geom	Facade Material	Occup	Avg
1xSV + TV	75.7	72.0	80.3	91.0	60.3	74.4	75.60
Up to 2xSV + TV	76.3	74.4	81.1	92.1	61.9	75.9	76.96
Up to 3xSV + TV	76.1	75.2	81.4	91.9	62.3	76.4	77.22
Up to 4xSV + TV	76.1	75.5	81.1	92.1	62.5	76.3	77.26
All SV + TV	76.0	75.6	81.3	91.9	62.4	76.6	77.28

Table 5: Impact of the maximum number of street-view images per example on model performance.

References

- Albert, A.; Kaur, J.; and Gonzalez, M. C. 2017. Using convolutional networks and satellite imagery to identify patterns in urban environments at a large scale. In *Proceedings of the 23rd ACM SIGKDD international conference on knowledge discovery and data mining*, 1357–1366.
- Basu, S.; Ganguly, S.; Mukhopadhyay, S.; DiBiano, R.; Karki, M.; and Nemani, R. 2015. DeepSAT: a learning framework for satellite imagery. In *Proceedings of the 23rd SIGSPATIAL international conference on advances in geographic information systems*, 1–10.
- Bódis-Szomorú, A.; Riemenschneider, H.; and Van Gool, L. 2016. Efficient volumetric fusion of airborne and street-side data for urban reconstruction. In *International Conference on Pattern Recognition*, 3204–3209. IEEE.
- Frohlich, B.; Rodner, E.; and Denzler, J. 2010. A fast approach for pixelwise labeling of facade images. In *2010 20th International Conference on Pattern Recognition*, 3029–3032. IEEE.
- Gadde, R.; Marlet, R.; and Paragios, N. 2016. Learning grammars for architecture-specific facade parsing. *International Journal of Computer Vision* 117(3): 290–316.
- Kang, J.; Körner, M.; Wang, Y.; Taubenböck, H.; and Zhu, X. X. 2018. Building instance classification using street view images. *ISPRS Journal of Photogrammetry and Remote Sensing* .
- Korč, F.; and Förstner, W. 2009. eTRIMS Image Database for Interpreting Images of Man-Made Scenes. Technical Report TR-IGG-P-2009-01, Dept. of Photogrammetry, University of Bonn.
- Lotte, R.; Haala, N.; Karpina, M.; Aragão, L.; Shimabukuro, Y.; et al. 2018. 3D Façade Labeling over Complex Scenarios: A Case Study Using Convolutional Neural Network and Structure-From-Motion. *Remote Sensing* .
- Riemenschneider, H.; Bódis-Szomorú, A.; Weissenberg, J.; and Van Gool, L. 2014. Learning where to classify in multi-view semantic segmentation. In *Proceedings of the European Conference on Computer Vision*, 516–532. Springer.
- Riemenschneider, H.; Krispel, U.; Thaller, W.; Donoser, M.; Havemann, S.; Fellner, D.; and Bischof, H. 2012. Irregular lattices for complex shape grammar facade parsing. In *Proceedings of the IEEE Conference on Computer Vision and Pattern Recognition*, 1640–1647. IEEE.
- Shao, H.; Svoboda, T.; and Van Gool, L. 2003. Zubud-zurich buildings database for image based recognition. *Computer Vision Lab, Swiss Federal Institute of Technology, Switzerland, Tech. Rep* 260(20): 6.
- Teboul, O.; Kokkinos, I.; Simon, L.; Koutsourakis, P.; and Paragios, N. 2011. Shape grammar parsing via reinforcement learning. In *Proceedings of the IEEE Conference on Computer Vision and Pattern Recognition*, 2273–2280. IEEE.
- Tyleček, R.; and Šára, R. 2013. Spatial pattern templates for recognition of objects with regular structure. In *German Conference on Pattern Recognition*, 364–374. Springer.
- Workman, S.; Souvenir, R.; and Jacobs, N. 2015. Wide-area image geolocalization with aerial reference imagery. In *Proceedings of the IEEE International Conference on Computer Vision*, 3961–3969.
- Workman, S.; Zhai, M.; Crandall, D. J.; and Jacobs, N. 2017. A Unified Model for Near and Remote Sensing. In *Proceedings of the IEEE International Conference on Computer Vision*, 2688–2697.
- Yang, Y.; and Newsam, S. 2010. Bag-of-visual-words and spatial extensions for land-use classification. In *Proceedings of the 18th SIGSPATIAL international conference on advances in geographic information systems*, 270–279.